Journal of Alloys and Compounds 863 (2021) 158731

Contents lists available at ScienceDirect

Journal of Alloys and Compounds

journal homepage: www.elsevier.com/locate/jalcom

Microwave-assisted hydrothermal synthesis of $CuWO_4$-palygorskite nanocomposite for enhanced visible photocatalytic response

A.E.B. Lima [a,*], R.Y.N. Reis [a,b], L.S. Ribeiro [c], L.K. Ribeiro [c], M. Assis [c], R.S. Santos [a,b], C.H.M. Fernandes [d], L.S. Cavalcante [b], E. Longo [c], J.A.O. Osajima [e], G.E. Luz Jr [a,b,**]

[a] Departament of Chemistry (DQ), Federal University of Piauí - UFPI, Teresina, Piauí 64049-550, Brazil
[b] PPGQ-GERATEC-DQ, State University of Piauí - UESPI, 2231 João Cabral Street, P.O. Box 381, Teresina, Piauí 64002-150, Brazil
[c] CDMF-UFSCar, Federal University of São Carlos, P.O. Box 676, São Carlos, São Paulo 13565-905, Brazil
[d] Electrochemical Research Laboratory (LAPE), Chemistry Department, Federal University of São Carlos - UFSCar, Washington Luis Road km 235, São Carlos, São Paulo 13566-905, Brazil
[e] Interdisciplinary Laboratory for Advanced Materials – LIMAV, UFPI, Teresina, Piauí 64049-550, Brazil

A R T I C L E I N F O

Article history:
Received 19 November 2020
Received in revised form 6 January 2021
Accepted 9 January 2021
Available online 13 January 2021

Keywords:
Pollutant degradation
Advanced oxidation processes
Semiconductor photocatalyst
Clay
Palygorskite
Nanocomposites
Emergent pollutants

A B S T R A C T

$CuWO_4$-Pal nanocomposite formed by copper (II) tungstate nanoparticles with palygorskite clay mineral (Pal) was synthesized via coprecipitation method followed by microwave-assisted hydrothermal technique and applied in the photodegradation of the antibiotic ciprofloxacin (CIP) using visible-light irradiation. The formation of $CuWO_4$-Pal nanocomposite was confirmed by XRD, Raman spectroscopy and DRIFT studies. X-ray photoelectron spectroscopy (XPS) and photoelectrochemical studies of the nanocomposite showed structural changes, which induced the formation of oxygen vacancies and better charge carrier mobility. Field emission scanning electron microscopy (FE–SEM) and transmission electron microscopy (TEM) images revealed the fibrous morphology of Pal as well as the control of $CuWO_4$ crystal growth with the formation of the nanocomposite. The CIP photodegradation was influenced by the adsorption power and the pH solution. $CuWO_4$-Pal exhibited 92% of CIP photodegradation and 50% of total organic carbon (TOC) removal using an initial concentration of 8 mg L^{-1} at pH 10 after 90 min. Together with the photoelectrochemical study, the scavengers used indicated that the hole (h^+) is the main oxidative species in CIP photodegradation.

1. Introduction

Many semiconductors have been widely studied as materials for conversion energy systems, such as solar cells, as well as used in the photocatalytic process for the obtention of hydrogen gas by water splitting. Semiconductors can also be used as photocatalysts for both organic pollutant degradation and CO_2 reduction [1]. The large-scale application of semiconductor oxides in energy conversion processes is still limited due to the low performance of such processes. In this context, studies have been carried out aiming to understand the mechanisms of performance of the semiconductors as well as propose strategies to improve the results obtained in each material application. In order to better understand the photocatalytic processes in water treatment, our research group has been investigating solar energy conversion from semiconductor oxides such as WO_3 [2,3], Ag_3PO_4 [4], $NiWO_4$ [5] and $CuWO_4$ [6].

In general, white semiconductor oxides, such as ZnO and TiO_2, are photoactive only when irradiated with ultraviolet light, a fact that limits their use under direct solar radiation [7]. On the other hand, most colored semiconductor oxides undergo photocorrosion during catalytic processes. However, recent research has shown that copper tungstate ($CuWO_4$) is a colored semiconductor material with excellent chemical stability over a wide pH range [8].

$CuWO_4$, a well-known n-type semiconductor, has been studied as a photocatalyst for both the removal of organic pollutants from water and the photoelectrochemical (PEC) water splitting [9–11]. Nevertheless, it has been widely shown that the electron-hole (e^-/h^+) pair recombination in this semiconductor due to empty Cu ($3d_{x^2-y^2}$) mid-gap states located in the conduction band negatively affects the electron mobility [12,13]. As a way to overcome this problem, strategic studies are necessary to improve the charge transport property of $CuWO_4$.

* Corresponding author.
** Corresponding author at: PPGQ-GERATEC-DQ, State University of Piauí - UESPI, 2231 João Cabral Street, P.O. Box 381, Teresina, Piauí 64002-150, Brazil.
E-mail addresses: alinebrandao08@gmail.com (A.E.B. Lima), geraldoeduardo@ccn.uespi.br (G.E. Luz).

https://doi.org/10.1016/j.jallcom.2021.158731
0925-8388/

Various alternatives, such as heterojunction formation, metallic ion dopants and nanocomposites, have been reported in an attempt to improve charge recombination and low carrier mobility [8,14,15]. The use of clay minerals in combination with metal oxides has proved to be a promising alternative to enhance adsorption properties and separate e^-/h^+ because of their large surface area, ion exchange capacity and other important properties [16,17]. Among clay minerals, palygorskite (Pal) fibrous clay–characterized by a hydrated aluminum silicate consisting of the connection of SiO_4 tetrahedrons and magnesium octahedral sheets forming an open channel structure [18]–has attractive properties for the construction of nanocomposites with metal oxides, including high surface area, adsorption ability and large content of silanol groups (≡SiOH) [19]. Therefore, the combination of $CuWO_4$ and Pal can result in a material with enhanced properties for photocatalytic applications.

Methods such as hydrothermal method, precipitation method, hydrolysis route, among others have been used for the preparation of composites with clay minerals and metal oxides [20–22]. The microwave-assisted hydrothermal synthesis is a green method that promotes particle size control capability, low temperature processing and short reaction time when compared to the conventional hydrothermal system [23]. In addition, the rapid and uniform heating generated by microwave radiation is significant for structural modifications [24].

Among the applications employing semiconductor oxides, advanced oxidative processes (AOPs) emerged as a potential, non-toxic way of environmental remediation. In general, this process consists of the oxidation of organic contaminant to carbon dioxide and water by reactive oxygen species (ROS) or by photogenerated holes (h^+) in the semiconductor valence band (VB) when irradiated by a suitable light source [25]. The ROS can be generated from either water or OH^- oxidation by h^+, or water reduction by photogenerated electrons in the semiconductor conduction band (CB) [26,27].

Some environmental problems, such as contamination of wastewater and increased bacterial resistance, are caused by the high use of antibiotics today. Ciprofloxacin (CIP) is a fluoroquinolone antibiotic extensively used for bacterial diseases in humans and animals that has been identified as an emerging contaminant [28]. Previous works indicate that the release of CIP through misuse, excretion and disposal of pharmaceutical waste into the environment can cause bacterial resistance, generating problems related to the low therapeutic efficacy of this antibiotic [29,30]. In addition, CIP is resistant to conventional methods used for the treatment of effluents. Thus, it is necessary to perform advanced studies regarding its removal from the wastewater [31].

In this work, we report for the first time the synthesis and photocatalytic activity of $CuWO_4$-Pal nanocomposite for the efficient photodegradation of such emerging contaminant under visible-light irradiation. The photocatalytic studies included the characterization of the structural, morphological and photoelectrochemical properties as well as the CIP photodegradation and the mechanism involved.

2. Experimental methods

2.1. Synthesis of $CuWO_4$ and $CuWO_4$-Pal

The preparation of the materials was made using both the co-precipitation (CP) and the microwave-assisted hydrothermal (MAH) methods. The $CuWO_4$ synthesis began with the chemical precipitation of the crystals in a solution using equimolar amounts (2.0 mM) of copper nitrate trihydrate ($Cu(NO_3)_2.3H_2O$, 99%, Sigma-Aldrich) and sodium tungstate dihydrate ($Na_2WO_4.2H_2O$, 99%, P.A.-A.C.S.) as precursors. The precursors were dissolved in deionized water (50 mL) and mixed, forming an amorphous $CuWO_4$ precipitate. Subsequently, the precipitate was placed in an ultrasonic bath for 10 min.

The Pal used for the synthesis of the nanocomposite was purchased from the company Coimbra, located in the state of Piauí in Brazil. The clay was initially purified with hydrogen peroxide for the removal of organic matter according to the methodology previously reported by co-authors [32], followed by washing with deionized water. Based on literature, Thiruppathi et al., [20], in this work, we studied only one constituent proportion in $CuWO_4$-Pal composite, 6 wt% of Pal. Then, 48 mg (6.0 wt%) of Pal powder were added to the $CuWO_4$ suspension (803 mg) under continuous stirring and sonication for 30 min subsequently, the reaction mixture was processed in a Teflon autoclave, closed and transferred inside a domestic microwave-hydrothermal system. The hydrothermal process was performed at 160 ºC for 18 min with a heating rate of 5 ºC/min and pressure inside the autoclave of 6 atm (2.45 GHz, maximum power of 800 W). Finally, the colloidal suspension formed was dried and heat-treated at 500 ºC for 30 min in a furnace.

2.2. Materials characterization

The structures of $CuWO_4$, $CuWO_4$-Pal and Pal were characterized by X-ray diffraction (XRD) in a Rigaku-DMax/2500PC (Japan) with Cu-Kα radiation (λ = 1.5406 Å) in the 2θ range from 10º to 110º at a scan rate of 0.02º/min. Micro-Raman spectroscopy was recorded with a Horiba Jobin-Yvon micro-spectrometer model LabRAM at room temperature in the 50–1000 cm^{-1} region using a He-Ne laser as the excitation source through an Olympus TM BX41 microscope operating at a wavelength of 512 nm and maximum output power of 5.9 mW. The diffuse reflectance infrared fourier transform (DRIFT) spectroscopy data were collected with a Bruker (EQUINOX 55) spectrophotometer.

In order to evaluate the chemical composition of the samples, X-ray photoelectron spectroscopy (XPS) analyses were carried out on a Scientia Omicron ESCA spectrometer (Germany) using a monochromatic X-ray source of Al Kα (1486.7 eV). All peaks were calibrated with reference to the C 1s at 284.3 eV.

The surface morphology was obtained by field emission scanning electron microscopy (FE–SEM) using a Supra 35-VP (Carl Zeiss, Germany) operating at 5 kV. The transmission electron microscopy (TEM) and high-resolution transmission electron microscopy (HR-TEM) images were obtained using a JEM-2100F LaB6 (Joel) microscope operating at 200 kV. To calculate the optical band gap (E_{BG}), UV-Vis spectroscopy analysis was performed on a Shimadzu UV-2600 spectrophotometer programmed to diffuse reflectance. The textural properties were recorded with an ASAP 2020 (Micromeritics) at a temperature of 77 K by N_2 adsorption/desorption isotherms using Brunauer–Emmett–Teller (BET) and Barrett–Joyner–Halenda (BJH) methodologies.

For the photoelectrochemical studies, $CuWO_4$ and $CuWO_4$-Pal film electrodes were prepared on FTO conducting glass (TCO22–7, Aldrich, 7 Ω/sq) through the dripping of the suspension of oxides previously obtained. The analyses were performed in a three-electrode system consisting of an electrode working as a photocatalytic film, a platinum plate counter electrode and an Ag/AgCl reference electrode [11]. The photocurrent and electrochemical impedance spectroscopy (EIS) measurements of the samples were performed with an Autolab potentiostat/galvanostat (MPGSTAT 302 N Metrohm). The EIS data were measured using an amplitude of 10 mV and frequency range of 10 kHz–0.1 Hz. The light source used was an LCS-100 solar simulator (Oriel, Newport, USA) with power of 100 mW cm^{-2} and AM1.5 filter. In addition, the differential pulse voltammetry (DPV) analyses were made with pulse amplitude of 50 mV, pulse width of 50 ms and interval time of 0,5 s

2.3. Photocatalytic activity for CIP photodegradation

The ciprofloxacin (CIP) photodegradation using $CuWO_4$ and $CuWO_4$-Pal was investigated under visible-light irradiation and monitored by UV-Vis spectroscopy (JASCO V-660, USA) and through total organic carbon (TOC) analysis. For this study, 50 mg of the photocatalyst was mixed with 50 mL of CIP (8 mg L^{-1}). Then, this suspension was sonicated for 5 min. Before irradiation, the system was maintained in the dark for 30 min to achieve the adsorption/desorption equilibrium. The suspension was subsequently irradiated under six lamps (Philips TL-D, 15 W) in a photo-reactor at 20 ºC under stirring.

To measure the CIP maximum absorption (275 nm), aliquots (2 mL) of the suspensions were collected and filtered using a PVDF syringe filter (0.2 µm) to remove crystals in suspension. To evaluate the effect of pH on the photodegradation, the pH of the CIP solution was adjusted with hydrochloric acid (HCl, 0.1 mol L^{-1}) and sodium hydroxide (NaOH, 0.1 mol L^{-1}). The surface charge modifications in different pHs were analyzed by zeta potential measurements using a Zetasizer NanoZS (Malvern, UK).

The mineralization (i.e. conversion to CO_2) was analyzed through TOC measurements using a GE Sieviers Innovox analyzer. The TOC determination was made after mixing a diluted volume of the treated sample with H_3PO_4 (6.0 mol L^{-1}) and $Na_2S_2O_8$ (30% m/v) as acidifying and oxidizing solutions, respectively.

In order to evaluate the influence of h^+ and ROS on the CIP photodegradation mechanism, photocatalytic tests were carried out with the following radical scavengers: tert-butanol (t-BuOH, 17 mL), ammonium oxalate (AO, 2.8 mg), ascorbic acid (AA, 3.5 mg) and silver nitrate ($AgNO_3$, 3.2 mg) for $^{\bullet}OH$, h^+, $O_2^{\bullet-}$ and e^-, respectively.

3. Results and discussion

3.1. Structure of $CuWO_4$ and CuWO4-Pal samples

3.1.1. XRD analysis

XRD patterns of $CuWO_4$, Pal and $CuWO_4$-Pal nanocomposite are shown in Fig. 1. For the $CuWO_4$, all diffraction peaks are in agreement with the Inorganic Crystal Structure Data (ICSD) card No. 16009, indicating triclinic structure and high periodicity [33]. The triclinic structure belongs to the $P\bar{1}$ space group, composed by distorted octahedral clusters of $[CuO_6]$ and $[WO_6]$. As to the Pal, the XRD pattern shows diffraction peaks at 2θ = 14.1º, 17.4º, 19.1º, 20.23º, 21.07º and 24.16º corresponding to the (200), (220), (20$\bar{1}$), (040), (111) and ($\bar{3}$11) planes, respectively, which are typical of this clay mineral [34,35]. In addition, the clay presents an intense peak at 26.7º, which is characteristic of the impurity of quartz in the Pal structure (AMCSD Nº 4664) [36].

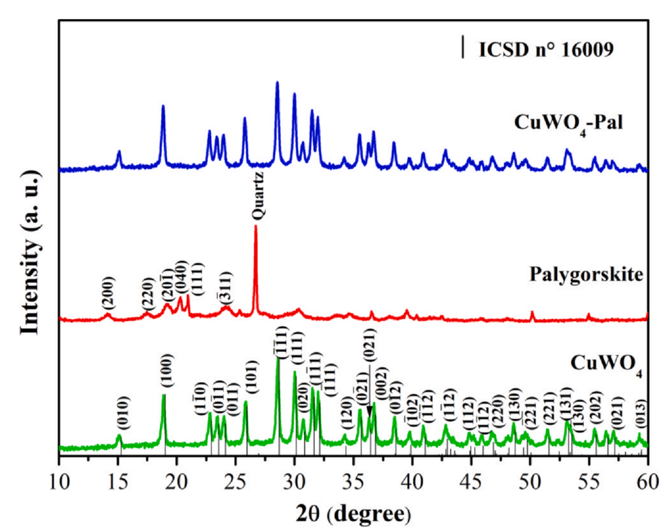

Fig. 1. XRD patterns of $CuWO_4$, Pal and $CuWO_4$-Pal samples and crystallographic card (ICSD No. 6009) for triclinic structure of $CuWO_4$.

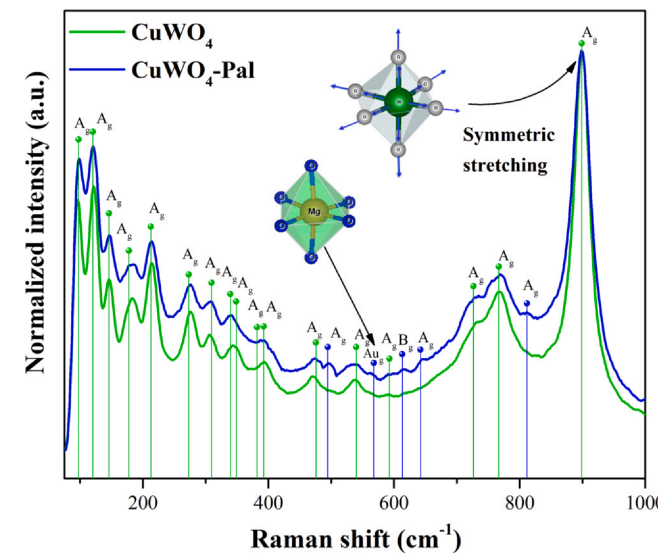

Fig. 2. Micro-Raman spectra of $CuWO_4$ and $CuWO_4$-Pal samples. The inset shows octahedral distortions of $[WO_6]$ and $[MgO_6]$ clusters.

No diffraction peaks of Pal can be seen in the nanocomposite XRD pattern, which can be related to the small Pal content in $CuWO_4$-Pal. However, the full width at half maximum (FWHM) value of the ($\bar{1}\bar{1}$1) peak of both $CuWO_4$ and $CuWO_4$-Pal samples indicates an increase from 0.26º to 0.29°, consequently causing a decrease in the crystallite size obtained by Scherrer's equation from 34.98 nm ($CuWO_4$) to 30.49 nm ($CuWO_4$-Pal). This behavior suggests an increase in the long-range disorder in the $CuWO_4$ structure caused by the addition of Pal, which may indicate nanocomposite formation. According to Wang et al., [37] Pal can provide active sites for the construction of various nanostructured materials, changing the local order/disorder.

3.1.2. Micro-Raman and DRIFT spectroscopy analyses

The micro-Raman spectra in the range of 50–1000 cm^{-1} of the $CuWO_4$ and $CuWO_4$-Pal nanocomposite are shown in Fig. 2. The $CuWO_4$ spectrum has 18 Raman-active vibration modes characteristic of the triclinic structure for this material, which is in agreement with our group theory calculation [38]. The symmetric stretching of O–W–O bonds at 900 cm^{-1} evidences short-range structural order of $CuWO_4$ crystals (inset of Fig. 2). The Raman spectrum of the nanocomposite exhibited modes predicted for the Pal structure. The modes located at 490, 638 and 810 cm^{-1} correspond to O–Si–O, O–Mg–O and Si–O–Si stretching modes of Pal, while those at 567 and 597 cm^{-1} are related to MgO_6 deformation (inset of Fig. 2), indicating interactions between $CuWO_4$ and Pal [39].

The DRIFT spectra of the $CuWO_4$ and $CuWO_4$-Pal nanocomposite are displayed in Fig. 3. Similar to the Raman spectra, it is possible to observe that the $CuWO_4$ presents 18 active different vibration modes in infrared. According to Fig. 3, the bands around 477 (O–Cu–O), 556 (O–W–O–W–O), 636, 756 (W–O) and 901 (O–W–O) cm^{-1} are related to vibrations of $CuWO_4$ octahedral clusters [33,40,41]. For the Pal, the band at 1030 cm^{-1} is associated with the presence of Si–O–Si bonds, while the band at 1215 cm^{-1} corresponds to the Si–O stretching vibration [42]. The band at 1638 cm^{-1} can be attributed to structural waters present in the Pal. Furthermore, the Pal displays a wide band around 3200–3710 cm^{-1} that can be related to stretching vibrations of the O–H groups in the clay (e.g. Si–OH, Fe–OH, Mg–OH and Al–OH) [43,44]. Comparing the DRIFT spectra of $CuWO_4$-Pal and $CuWO_4$, the formation of the nanocomposite can be demonstrated by the peaks typical of Pal located near 1215, 1638 and 3592 cm^{-1}. The band at 3582 cm^{-1} can also be attributed to silanol groups (≡SiO–H) located at the external surface of the Pal, which can serve

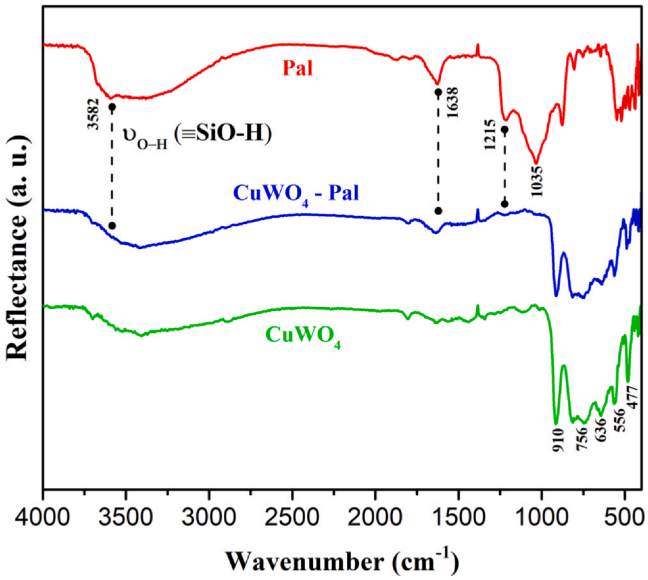

Fig. 3. DRIFT spectra of PAL, $CuWO_4$ and $CuWO_4$-Pal nanocomposite.

as active sites for the construction of nanocomposite materials [37,45]. In addition, the spectrum of the nanocomposite shows a decrease in the intensity of the $CuWO_4$ characteristic bands, suggesting the successful formation of $CuWO_4$-Pal. The DRIFT results corroborate the data from the Raman spectra and XRD patterns.

3.2. Surface properties

The XPS analysis was performed to assess the elemental composition of the sample surface as well as possible changes in the chemical state of elements due to nanocomposite formation. The XPS survey spectra of the $CuWO_4$ and $CuWO_4$-Pal indicated similar spectra in the presence of Cu, W and O, while the nanocomposite presented additional elements of Si, Al, Mn and Mg, confirming the characteristic peaks of Pal (Fig. 4(a)). The binding energies were corrected for the position of C 1s (284.3 eV).

Fig. 4(b–d) illustrates the high-resolution energy spectra for both samples as well as the chemical state of each element. Fig. 4(b) shows binding energies relative to electronic states of $Cu2p_{3/2}$ (934.9 eV) and $Cu2p_{1/2}$ (954.0 eV). In addition, the spectra also revealed two satellite peaks (961.4 and 941.8 eV) that are consistent with Cu^{2+} (partially filled 3d-orbital) in the $CuWO_4$ structure [14,46]. The high-resolution of W4f showed three deconvoluted peaks in this region, indicating the valence state of W^{6+} characteristic of W $4f_{7/2}$

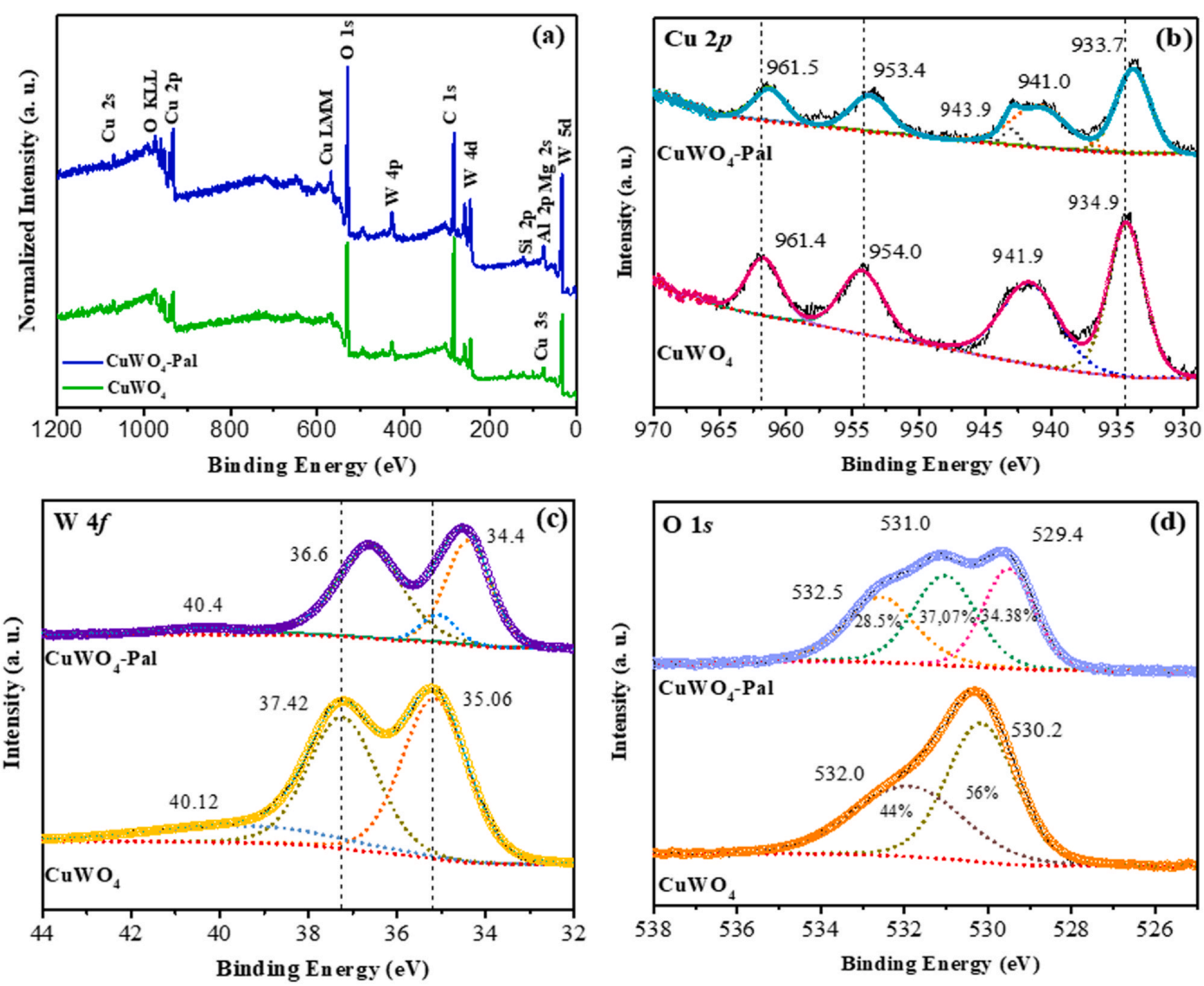

Fig. 4. (a) XPS survey spectra and high-resolution (b) Cu 2p, (c) W 4f and (d) O 1s of both $CuWO_4$ and $CuWO_4$-Pal.

(35.06 eV), W $4f_{5/2}$ (37.42 eV) and W $5p_{3/2}$ (40.12 eV) levels (Fig. 4(c)) [47]. By comparing the spectra, it was possible to note that the $CuWO_4$-Pal exhibited a shift to lower binding energy, demonstrating the existence of W^{5+} (34.4 eV and 36.7 eV) and Cu^+ (953.4 eV and 933.7 eV) chemical states and the emergence of oxygen vacancies, which can be attributed to the doping of $CuWO_4$ by chemical elements present in the Pal (e.g. Fe, Mg, Al) [48,49]. Fig. 4(d) shows two peaks for the O 1s region at 530.2 eV and 532 eV attributed to Cu–O groups and surface hydroxide (O-H), respectively. The nanocomposite revealed one additional peak at 531 eV, which can be assigned to hydroxyl groups of the Pal [50]. The doping effects in the nanocomposite induced an increase in the oxygen vacancies, improving the charge transport property and catalyst activity [49,51].

3.3. UV-Vis DRS analysis and sample morphology

The optical band gap energy (E_{BG}) of the $CuWO_4$ and $CuWO_4$-Pal was calculated by the Kubelka–Munk function, assuming an indirect optical transition $(F(R_\infty)\ x\ h\nu)^{1/2}$ (see Fig. SM1) [52]. The $CuWO_4$ nanocrystals exhibited an E_{BG} value of approximately 2.26 eV, similar to that reported in the literature [53,54]. The absorption spectrum for the $CuWO_4$-Pal displayed a small shift for a longer wavelength, indicating transition energies of 2.15 eV. The insertion of Pal caused enhanced visible-light absorption attributed to the modification in the nanocomposite electronic structure, which can be attributed to the doping of $CuWO_4$ by metals from the Pal structure, as previously indicated by XPS and Raman results [17]. This behavior suggests the formation of the $CuWO_4$-Pal with improved optical and catalytic properties in relation to the $CuWO_4$ [55,56].

Fig. 5(a–d) shows the morphology of the $CuWO_4$, Pal and $CuWO_4$-Pal. Fig. 5(a) reveals the presence of $CuWO_4$ nanocrystals with an average size of approximately 58 ± 13 nm (Fig. 5b). Fig. 5(c) indicates that the Pal presented a fibrous needle-like morphology [57] with an average size of 970 ± 24 nm and aspect ratio of 8.3 ± 2. In the case of the $CuWO_4$-Pal nanocomposite, the particle average size decreased to 38 ± 8 nm (Fig. 5f), corroborating the results on the crystallite sizes obtained by the Scherrer's equation. This behavior reveals that the $CuWO_4$ crystal size was controlled by its interaction with Pal. Similar results for a Pal/Ag_3PO_4 nanocomposite were reported by Luo et al. [21], who showed that the Pal has properties such as negative surface charge and rheological behavior that can control crystal growth. The crystal size reduction may promote an increase in the photocatalyst surface area and improve its photocatalytic properties [57].

The TEM and HR–TEM images of the $CuWO_4$-Pal (Fig. 6a–c) confirmed the nanocomposite formation through the interaction of the $CuWO_4$ crystals with the fibrous Pal. It can be observed that the nanocomposite improved the surface area and contributed to increased catalytic efficiency [58]. In Fig. 7(c), it is possible to note the presence of nanocrystals with defined planes. The selected area shows interplanar distances of 0.31 nm, 0.360, 0.261, 0.153, 0.184, 0.379, 0.281, 0.141, 0.218, 0.243 and 0.210 nm associated with the $(\bar{1}\bar{1}1)$, (011), (120), (231), $(\bar{2}\bar{2}1)$, $(0\bar{1}1)$, $(\bar{1}11)$, $(\bar{2}22)$, $(\bar{1}02)$, (002) and $(\bar{1}21)$ planes, respectively (inset of Fig. 6c). These planes reinforce the $CuWO_4$ triclinic structure observed by XRD and Raman analyses.

3.4. Textural properties

Fig. 7(a) illustrates the N_2 adsorption/desorption analysis for the Pal, $CuWO_4$ and $CuWO_4$-Pal. The curves show type II isotherms with H3 hysteresis loop [59,60], associated to interstitial spaces between particles that lead a wide range of pore diameter, as shown in Fig. 7(b). Table 1 exhibits BET specific surface area, pore volume and average pore diameter values for all samples. As it can be seen, the incorporation of Pal into the $CuWO_4$ improved the surface area when compared to the pure $CuWO_4$. Moreover, the enhancement of surface area may also be related to the smaller particle sizes of the nanocomposite (as seen in Fig. 5). The pore diameter distributions were estimated using the Barrett–Joyner–Halenda (BJH) method (Fig. 7b). The nanocomposite showed an increase in the pore volume in relation to pure $CuWO_4$ that can improve a pollutant adsorption. Generally, a photocatalyst with large surface area and high pore volume promotes more exposed surface sites for adsorption [55]. Therefore, the $CuWO_4$-Pal can demonstrate better adsorption and photocatalytic activity than the $CuWO_4$ crystals.

3.5. Photoelectrochemical studies of $CuWO_4$ and $CuWO_4$-Pal

The photoelectrochemical studies of the films prepared with $CuWO_4$ and $CuWO_4$-Pal samples were investigated in aqueous solutions of Na_2SO_4 (0.1 mol L^{-1}) as the supporting electrolyte. The charge transfer resistance and photocurrent measurements were obtained using electrochemical impedance spectroscopy (EIS) and linear sweep voltammetry (LSV).

The Nyquist plots for the $CuWO_4$ and $CuWO_4$-Pal are given in Fig. 8(a). As expected, the studies show that the nanocomposite has a lower resistance in the charge transport than the $CuWO_4$, which is represented by the smaller semicircle [61]. This behavior is confirmed by the linear sweep voltammograms obtained at 5 mV/s under chopped illumination. The voltammograms shown in Fig. 8(b) exhibit an increased photocurrent response for the $CuWO_4$-Pal due to the doped $CuWO_4$, which in turn induced oxygen vacancies and enhanced the charge carrier mobility. The presence of oxygen vacancies in the nanocomposite can be evidenced by the emergence of W^{5+} and Cu^+ species, as previously discussed based on the XPS studies [62,63]. The efficient separation of charge carriers allows a longer lifetime for the active species available in the photocatalytic activity. This behavior was also reported in the literature with the preparation of composites using Pal and other semiconductor oxides [17,22,64].

3.6. Photocatalytic performance

The pH plays as important role in the adsorption of pollutants on the catalyst surface and in the photodegradation efficiency [65]. The CIP photodegradation tests were carried out on $CuWO_4$-Pal samples with different pHs. The dark adsorption/desorption equilibrium was reached after 30 min. As it can be seen in Fig. 9(a), the CIP adsorption on $CuWO_4$-Pal increased from pH 3 to pH 7 and decreased in pH 10. The adsorption processes were influenced by electrostatic interaction between the photocatalyst surface charge and the organic molecule. To better understand this behavior, zeta potential measurements were performed for CIP and photocatalysts (Fig. SM2). According to the literature [66,67], CIP is a compound that has two pK_a values (see inset of Fig. 9a), which are associated with the carboxylic group (pK_{a1} = 6.1) and nitrogen on the piperazinyl ring (pK_{a2} = 8.7); in acidic conditions, CIP has as a protonated form, while in alkaline conditions it has a deprotonated form (see zeta potential of CIP, Fig. SM2) [68]. In addition, CIP is characterized by the zwitterionic form between pH 6.1 and 8.7. In this condition, the molecule presents an equal charge distribution between the protonated ($^+NH_2$) and deprotonated (COO^-) groups [69].

For the nanocomposite, the maximum adsorption was observed at pH 7.0, which corresponds to the zwitterionic form. It can imply that the positively charged ($^+NH_2$) groups of the CIP molecules will be electrostatically attracted by the negative charge surface of the $CuWO_4$, which is confirmed by its zeta potential behavior as a function of pH (Fig. SM2b). The low CIP adsorption on the $CuWO_4$-Pal at pH 3.0 was not expected since the predominant CIP species in this pH is cationic. However, the electrostatic attraction can be prevented due to high concentrations of H^+ ions that compete with

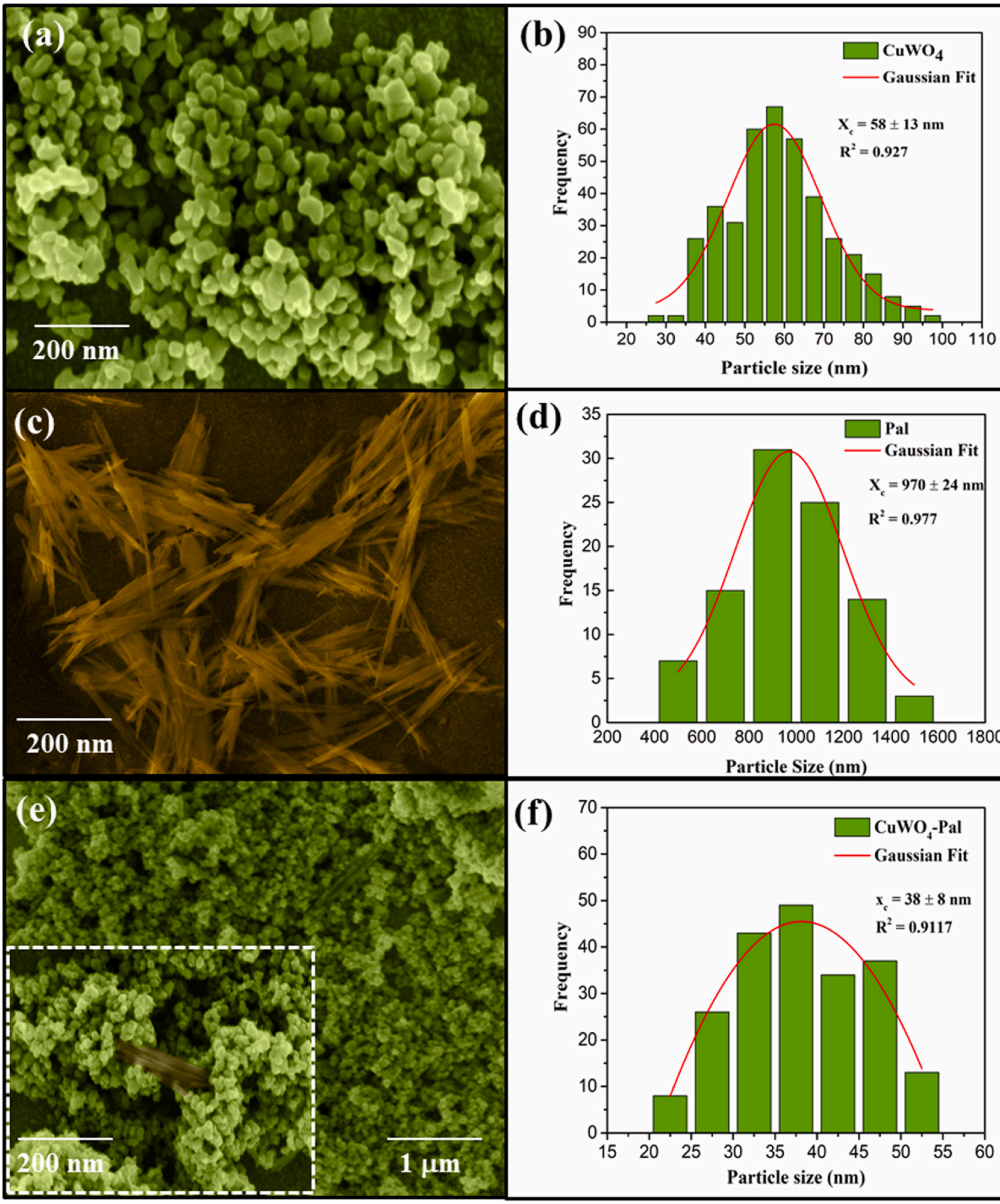

Fig. 5. FE-SEM images and average particle size distribution of (a and b) $CuWO_4$, (c and d) Pal and (e and f) $CuWO_4$-Pal.

the positive charge of CIP [70]. At pH 10.0, the decrease in adsorption is related to an electrostatic repulsion between the $CuWO_4$-Pal surface charges and the deprotonated CIP molecules. This behavior was also previously studied by Berhane et al., [71] who reported the CIP adsorption on palygorskite and montmorillonite. The authors showed that Pal also has a negative charge surface in alkaline medium, causing an electrostatic repulsion in the CIP adsorption.

After the adsorption equilibrium was reached, the photocatalyst was irradiated with visible light, when it was possible to observe an increase in the degradation efficiency under alkaline conditions (pH 10 = 92% after 90 min of irradiation), while the lowest degradation was seen at pH 3.0 (55%). Although the adsorption was higher at pH 7.0, the best degradation rate was obtained under alkaline conditions, which can be attributed to the increased production of

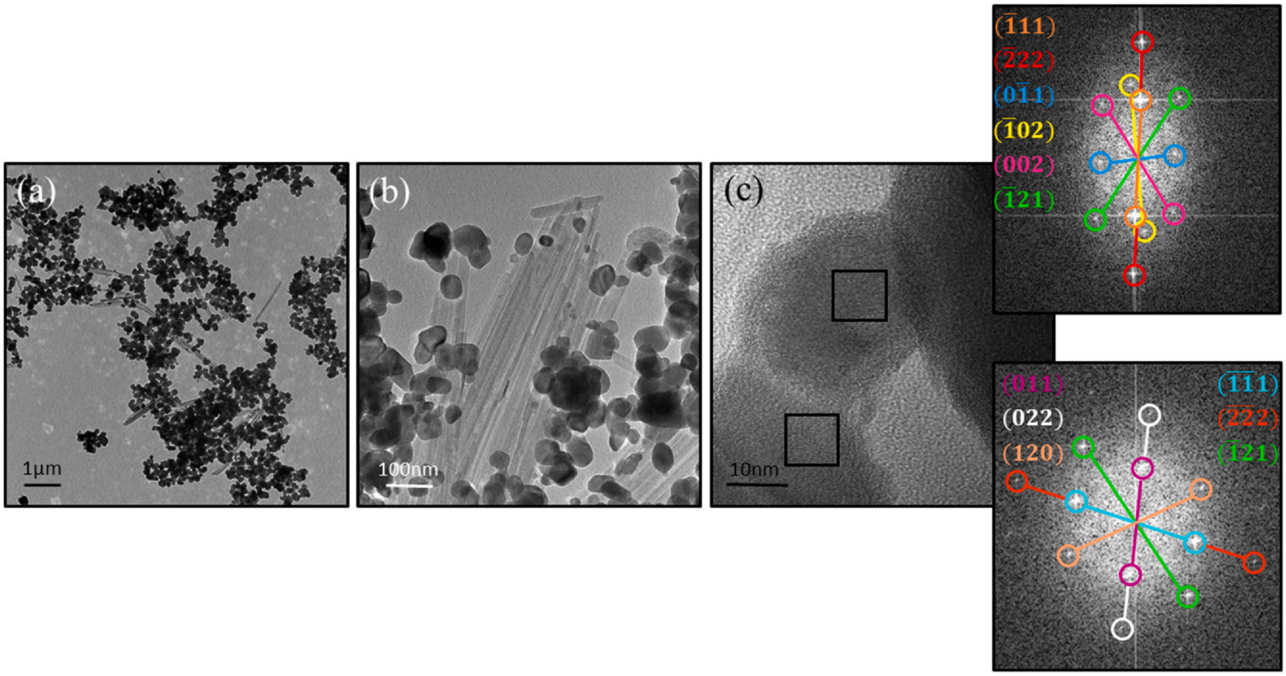

Fig. 6. (a) TEM image of $CuWO_4$-Pal, (b) high magnification of the nanocomposite and (c) HR-TEM for $CuWO_4$ nanocrystals.

hydroxyl radicals (•*OH*) in the solution [65]. Thus, pH 10 presented the best photodegradation condition for CIP on the $CuWO_4$-Pal.

The pH effect was important because it showed different properties for the same material. For example, at pH 7 it was possible to observe an adsorptive process greater than the photocatalytic process. The reverse behavior was observed at pH 3, when a lower adsorption of the material was noted. In the case of pH 10, there was a synergistic effect of both processes, i.e, the occurrence of both photocatalytic activity and pollutant adsorption. This combination is essential for materials that can be applied in environmental remediation, justifying the choice of such material for tests with scavengers and TOC analysis, as seen in Fig. 9(b–d).

Fig. 9(b) presents a comparison of the CIP degradation for the photocatalysts and photolysis at pH 10. It can be observed that the photolysis removed only 8% of CIP. In contrast, the $CuWO_4$ presented a photodegradation efficiency of 80%, while the nanocomposite degraded 92% of CIP. The $CuWO_4$ showed a photocatalytic efficiency superior to the photodegradation studies reported in the literature for this material [15]. This can be explained by the large pore volume obtained by microwave assisted-hydrothermal synthesis, which favored the adsorption and photocatalytic response [72]. For the $CuWO_4$-Pal, in addition to the large volume of pores, the increase in the specific surface area and the efficient separation of charge carriers induced enhanced photocatalytic activity.

Table 1
Textural properties of Pal, $CuWO_4$ and $CuWO_4$-Pal.

Sample	Specific surface Area (m^2/g)	Pore Volume (cm^3/g)	Pore Diameter (nm)
Pal	82	0.28	19.8
$CuWO_4$	12	0.11	63.6
$CuWO_4$-Pal	18	0.16	45.6

The mineralization of CIP was evaluated through total organic carbon (TOC), as shown in Fig. 9(c). The $CuWO_4$-Pal photocatalyst reached approximately 50% of drug removal, while for the $CuWO_4$

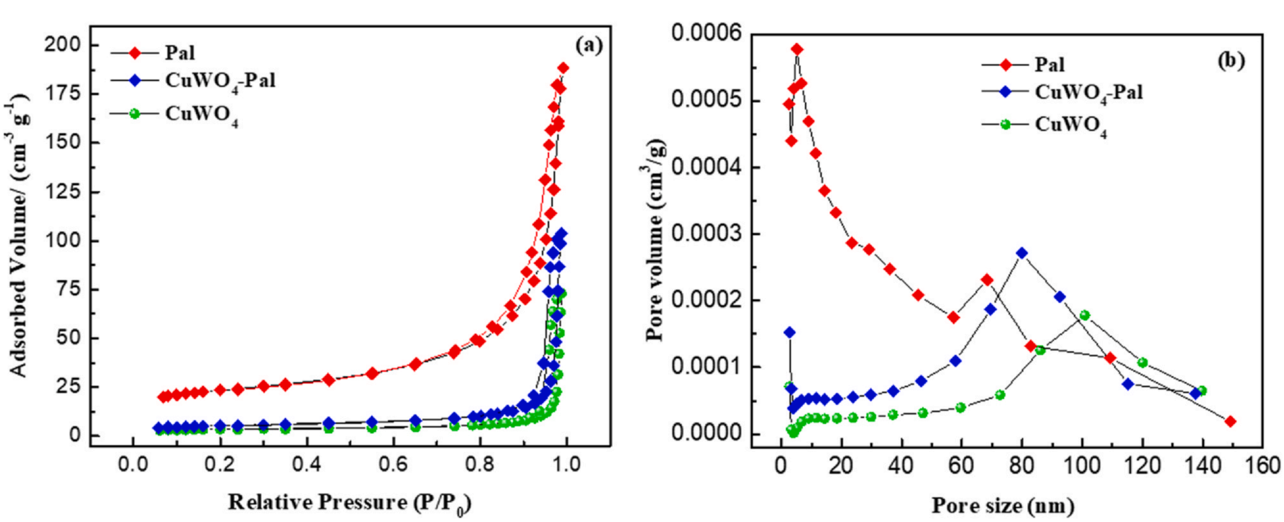

Fig. 7. (a) N_2 adsorption/desorption isotherms and (b) BJH pore diameter distribution plots for $CuWO_4$, $CuWO_4$-Pal and Pal.

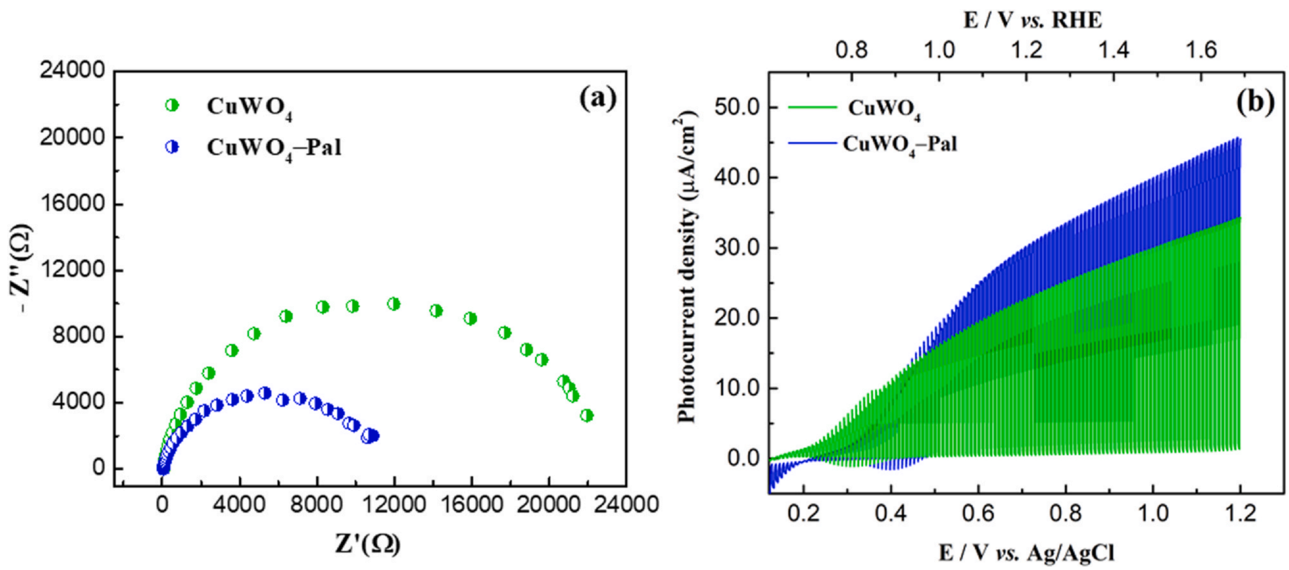

Fig. 8. (a) Nyquist plots and (b) linear sweep voltammetry under chopped light illumination for $CuWO_4$ and $CuWO_4$-Pal irradiated by a solar simulator.

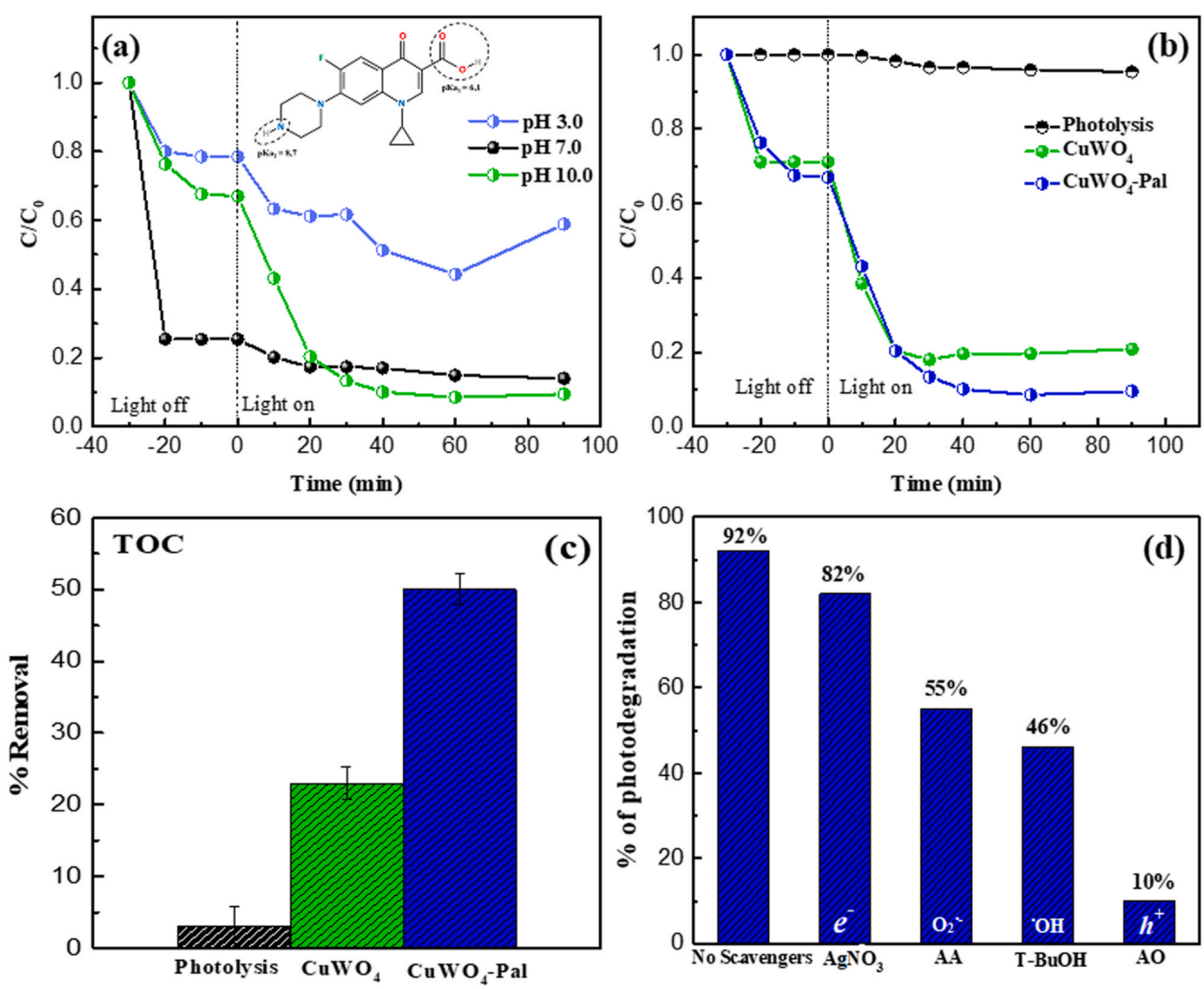

Fig. 9. (a) Effects of pH on the photodegradation of CIP using the $CuWO_4$-Pal nanocomposite, (b) photodegradation curves of CIP in the absence of photocatalysts and presence of $CuWO_4$ and $CuWO_4$-Pal, (c) mineralization monitored by TOC, and (d) effect of scavenges on the CIP photodegradation in the presence of $CuWO_4$-Pal.

this value was only 24%. The mineralization activity was lower than that suggested by the UV-Vis analysis (Fig. 9b), probably due to possible intermediate molecules generated in the photocatalytic process, as discussed in previous studies [60].

Photocatalytic degradation involves different oxidative species generated by the absorption of light on the photocatalyst surface, such as e^-, h^+, $^{\bullet}OH$ and superoxide radical ($O_2^{\bullet-}$) [15,73]. In order to evaluate the active species in the CIP degradation process on the $CuWO_4$-Pal, measurements with radical scavengers using *tert*-butanol (*t*-BuOH), ammonium oxalate (AO), ascorbic acid (AA) and silver nitrate ($AgNO_3$) were performed. Fig. 9(d) shows that the h^+ and •OH radicals play a major role in the CIP photodegradation. Furthermore, the degradation efficiency was considerably suppressed by AO, indicating that the h^+ and $^{\bullet}OH$ radicals on the nanocomposite surface are fundamental to the process. These active species can act in two ways: direct oxidation of CIP or production of hydroxyl radicals through reaction with the water molecule [74].

3.7. Photocatalytic mechanism

The energy diagram was proposed based on the photoelectrochemical studies and UV-Vis absorption, considering the positions of the conduction band (CB) and valence band (VB) for the photocatalysts, and the LUMO (lowest unoccupied molecular orbital) and HOMO (highest occupied molecular orbital) energy levels for the CIP molecule. The diagram brings important information regarding the charge separation mechanisms and reactive species for the photocatalytic activity.

The positions of the CB and VB of the semiconductors were estimated using the E_{BG} and flat band potential (E_{fb}) measurements. For the semiconductors, the E_{fb} may be related to the Fermi energy level [75]. In the case of an n-type semiconductor, the E_{fb} can be associated with the CB position. The E_{fb} values were calculated from the photocurrent curves presented in Fig. 8(b), as briefly described in the Supplementary Material (Fig. SM3). The E_{fb} for the $CuWO_4$ and $CuWO_4$-Pal films was estimated at 0.28 and 0.37 V, respectively. The CB was then calculated by converting the E_{fb} values to energy on the vacuum scale using Eq. 1:

$$[E(eV) = -4.5eV - eE_{RHE}(V)], \tag{1}$$

where e is the electron charge and E_{RHE} is the potential of the reversible hydrogen electrode [2]. The CB position for the $CuWO_4$ and $CuWO_4$-Pal corresponds to −5.31 and −5.34 eV, respectively. The energy range between the CB and the VB should approximately correspond to the E_{BG} of the semiconductors. Considering the E_{BG} values previously estimated for the $CuWO_4$ and $CuWO_4$-Pal samples (Fig. SM1), the positions of the VB for the photocatalysts were found to be −7.81 and −7.54 eV, respectively.

DPV measurements were carried out to estimate the HOMO energy level of CIP (Fig. SM4). The redox potential for CIP oxidation was about 1.50 V. Therefore, the calculated HOMO energy level of CIP was −6.39 eV. On the other hand, the LUMO energy level was determined by UV-Vis measurements (see inset of Fig. SM4). The bands observed at 276 and 322 nm were converted considering the energy $\left[E(eV) = \frac{1241}{l}(nm)\right]$ and estimated in the range of 4.51–3.85 eV. The position of the HOMO and LUMO energy levels are in accordance with that estimated by density functional theory (DFT) for the CIP molecule [76].

Fig. 10 illustrates the energy diagram constructed for the CIP molecule and photocatalysts. After absorbing radiation with adequate energy, the charge carriers are generated in the semiconductor surface. The appropriate position of the HOMO and LUMO energy levels of the molecule in relation to the conduction and valence bands of the semiconductor may favor the photodegradation of pollutants by photogenerated h^+ in the VB of the photocatalyst

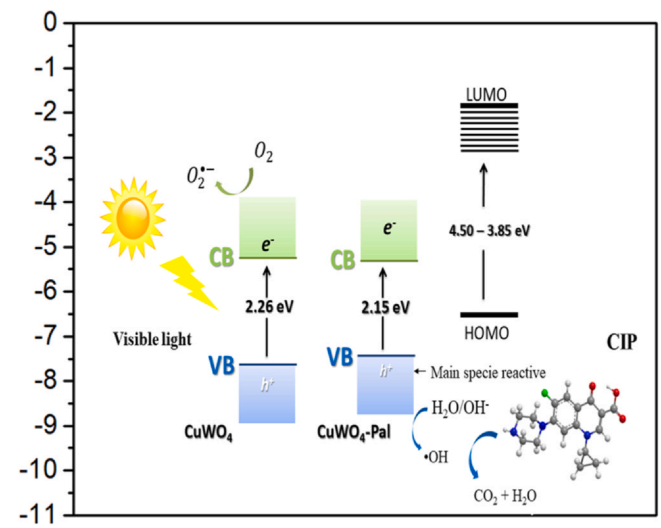

Fig. 10. Energy diagram for the valence and conduction band positions of $CuWO_4$, $CuWO_4$-Pal, and HOMO and LUMO energy levels of CIP.

[77,78]. In this figure, it is also possible to observe that the HOMO energy level of CIP is between the CB and the VB of the $CuWO_4$ and $CuWO_4$-Pal indicating that the oxidation of CIP by h^+ using the nanocomposite was favored.

The CIP photodegradation steps can be explained based on the results of active species and the energy diagram constructed. First, the $CuWO_4$-Pal is irradiated using visible light at alkaline pH (E_{BG} = 2.15 eV), consequently promoting charge separation ($e^- - h^+$) pairs (Eq. 2) [51]. The electron excited in the CB of the photocatalyst can react with oxygen gas adsorbed on its surface and form the superoxide radical ($O_2^{\bullet-}$) with strong oxidative capacity (Eq. 3). As previously discussed, the position of the VB of $CuWO_4$-Pal in relation to the HOMO energy level is favorable to the oxidation of CIP through the photogenerated h^+. In addition, the h^+ radical can also participate in the catalytic activity through reactions with OH^- ions present in the alkaline medium, which promote the generation of $^{\bullet}OH$. This process suggests a high photocatalytic efficiency due to the inhibition of the recombination of e^-/h^+ pairs [78,79]. The $O_2^{\cdot-}$ and h^+ radicals continue to result in active species, such as H_2O_2 and $^{\cdot}OH$, from reactions with H_2O and H^+ ions present in the medium (Eqs. 4–8) [80,81].

$$CuWO_4 - PAL + hv \rightarrow CuWO_4 - PAL + (e^- - h^+) \tag{2}$$

$$e^- + O_2 \rightarrow O_2^{\cdot-} \tag{3}$$

$$h^+ + H_2O \rightarrow {}^{\cdot}OH + H^+ \tag{4}$$

$$O_2^{\cdot-} + H^+ \rightarrow O_2H^{\cdot} \tag{5}$$

$$2O_2H^{\cdot} \rightarrow H_2O_2 + O_2 \tag{6}$$

$$H_2O_2 + e^- \rightarrow {}^{\cdot}OH + OH^- \tag{7}$$

$$H_2O_2 + {}^{\cdot}OH + O_2H^{\cdot} + O_2^{\cdot-} + CIP \rightarrow CO_2 + H_2O \tag{8}$$

4. Conclusions

In summary, $CuWO_4$-Pal nanocomposite was prepared by the coprecipitation method followed by the microwave-assisted hydrothermal synthesis. The characterization results indicated the presence of the triclinic $CuWO_4$ as well as the successful formation of the $CuWO_4$-Pal. XPS studies revealed structural changes in the nanocomposite, which induced the emergence of oxygen vacancies that improved the charge carrier mobility. The $CuWO_4$-Pal showed increased absorption of visible light (E_{BG} = 2.15 eV), forming a nanocomposite with enhanced photocatalytic performance and mineralization. The degradation of the CIP solution by $CuWO_4$-Pal using visible-light irradiation was approximately 92% after 90 min. This behavior was due to the increase in surface area and greater charge mobility of the $CuWO_4$ after the incorporation of the Pal. Catalytic tests with radical scavengers showed that h^+ was the main oxidative species present in the CIP degradation. Additionally, the energy diagram constructed suggested that the CIP can be oxidized by photogenerated holes in the VB of the photocatalyst. These results indicate the CuWO4-Pal nanocomposite proved to be a photocatalyst potential to mineralize other organic pollutants such as resistant drugs, herbicides and dyes.

CRediT authorship contribution statement

A.E.B. Lima: Conceptualization, Formal analysis, Investigation, Methodology, Resources, Writing - original draft. **R.Y.N. Reis:** Investigation, Methodology, Resources. **L.S. Ribeiro:** Investigation, Resources. **L.K. Ribeiro:** Investigation, Resources. **M. Assis:** Formal analysis, Investigation, Resources. **R.S. Santos:** Conceptualization, Methodology, Writing - original draft. **C.H.M. Fernandes:** Investigation, Resources. **L.S. Cavalcante:** Conceptualization, Funding acquisition, Writing - original draft. **E. Longo:** Funding acquisition, Supervision. **J.A.O. Osajima:** Conceptualization, Writing - review & editing. **G.E. Luz Jr:** Conceptualization, Funding acquisition, Methodology, Project administration, Supervision, Writing - review & editing.

Declaration of Competing Interest

The authors declare that they have no known competing financial interests or personal relationships that could have appeared to influence the work reported in this paper.

Acknowledgments

This work was financially supported by the following funding agencies: FAPEPI, CAPES (006/2018), CNPq (455864/2014-4, 307559/2015-7, 307559/2016-8, 305757/2018-0 and 166281/2017-4), FINEP (ref. No. 0315/08) and FAPESP (2013/07296-2). The authors also thank the laboratory assistance provided by Rede Agronano-EMBRAPA for the BET analysis.

Appendix A. Supporting information

Supplementary data associated with this article can be found in the online version at doi:10.1016/j.jallcom.2021.158731.

References

[1] J. Luo, S. Zhang, M. Sun, L. Yang, S. Luo, J.C. Crittenden, A critical review on energy conversion and environmental remediation of photocatalysts with remodeling crystal lattice, surface, and interface, ACS Nano 13 (2019) 9811–9840, https://doi.org/10.1021/acsnano.9b03649
[2] M.J.S. Costa, G.S. Costa, A.E.B. Lima, G.E.L. Jr, E. Longo, L.S. Cavalcante, R.S. Santos, Photocurrent response and progesterone degradation by employing WO3 films modified with platinum and silver nanoparticles, ChemPlusChem 83 (2018) 1153–1161, https://doi.org/10.1002/cplu.201800534
[3] M.S. Lima, J.F. Cruz-Filho, L.F.G. Noleto, L.J. Silva, T.M.S. Costa, G.E. Luz, Synthesis, characterization and catalytic activity of Fe_3O_4@WO_3/SBA-15 on photodegradation of the acid dichlorophenoxyacetic (2,4-D) under UV irradiation, J. Environ. Chem. Eng. 8 (2020) 104145, https://doi.org/10.1016/j.jece.2020.104145
[4] T.M.S. Costa, M.S. Lima, J.F. Cruz Filho, L.J. Silva, R.S. Santos, G.E. Luz, Synthesis, characterization, and photocatalytic activity of Ag_3PO_4/SBA-15 in ciprofloxacin degradation under polychromatic irradiation, J. Photochem. Photobiol. A Chem. 364 (2018) 461–471, https://doi.org/10.1016/j.jphotochem.2018.06.039
[5] F.J.O. Rosal, A.F. Gouveia, J.C. Sczancoski, P.S. Lemos, E. Longo, B. Zhang, L.S. Cavalcante, Electronic structure, growth mechanism, and sonophotocatalytic properties of sphere-like self-assembled $NiWO_4$ nanocrystals, Inorg. Chem. Commun. 98 (2018) 34–40, https://doi.org/10.1016/j.inoche.2018.10.001
[6] A.E.B. Lima, R.Y.N. Reis, M.J. dos, S. Costa, J.P.C. Moura, L.J. da Silva, R. da, S. Santos, L.S. Cavalcante, E.L. da Silva, G.E. da Luz Júnior, Photoelectrocatalysis properties of cuwo4 porous film under polychromatic light, Estudos Interdisciplinares Nas Ciências Exatas e Da Terra e Engenharias 2, Atena Editora, 2019, pp. 374–383, , https://doi.org/10.22533/at.ed.648191030935
[7] A.H. Zyoud, A. Zubi, S. Hejjawi, S.H. Zyoud, M.H. Helal, S.H. Zyoud, N. Qamhieh, A.R. Hajamohideen, H.S. Hilal, Removal of acetaminophen from water by simulated solar light photodegradation with ZnO and TiO_2 nanoparticles: catalytic efficiency assessment for future prospects, J. Environ. Chem. Eng. 8 (2020) 104038, https://doi.org/10.1016/j.jece.2020.104038
[8] J.P.C. Moura, R.Y.N. Reis, A.E.B. Lima, R.S. Santos, G.E. Luz, Improved photoelectrocatalytic properties of ZnO/$CuWO_4$ heterojunction film for RhB degradation, J. Photochem. Photobiol. A Chem. 401 (2020) 112778, https://doi.org/10.1016/j.jphotochem.2020.112778
[9] A. Habibi-Yangjeh, M. Mousavi, Deposition of $CuWO_4$ nanoparticles over g-C3N4/Fe3O4 nanocomposite: novel magnetic photocatalysts with drastically enhanced performance under visible-light, Adv. Powder Technol. 29 (2018) 1379–1392, https://doi.org/10.1016/j.apt.2018.02.034
[10] J. Yang, C. Li, P. Diao, Molybdenum doped $CuWO_4$ nanoflake array films as an efficient photoanode for solar water splitting, Electrochim. Acta 308 (2019) 195–205, https://doi.org/10.1016/j.electacta.2019.04.044
[11] A.E.B. Lima, M.J.S. Costa, R.S. Santos, N.C. Batista, L.S. Cavalcante, E. Longo, G.E. Luz, Facile preparation of $CuWO_4$ porous films and their photoelectrochemical properties, Electrochim. Acta 256 (2017) 139–145, https://doi.org/10.1016/j.electacta.2017.10.010
[12] J.E. Yourey, K.J. Pyper, J.B. Kurtz, B.M. Bartlett, Chemical stability of $CuWO_4$ for photoelectrochemical water oxidation, J. Phys. Chem. C 117 (2013) 8708–8718, https://doi.org/10.1021/jp402048b
[13] K. Dashtian, M. Ghaedi, H. Shirinzadeh, S. Hajati, S. Shahbazi, Achieving enhanced blue-light-driven photocatalysis using nanosword-like VO_2/$CuWO_4$ type II n–n heterojunction, Chem. Eng. J. 339 (2018) 189–203, https://doi.org/10.1016/j.cej.2018.01.107
[14] R. Huang, X. Gu, W. Sun, L. Chen, Q. Du, X. Guo, J. Li, M. Zhang, C. Li, In situ synthesis of Cu^+ self-doped CuWO4/g-C3N4 heterogeneous Fenton-like catalysts: the key role of Cu^+ in enhancing catalytic performance, Sep. Purif. Technol. 250 (2020) 117–174, https://doi.org/10.1016/j.seppur.2020.117174
[15] M. Thiruppathi, J. Vinoth Kumar, M. Vahini, C. Ramalingan, E.R. Nagarajan, A study on divergent functional properties of sphere-like $CuWO_4$ anchored on 2D graphene oxide sheets towards the photocatalysis of ciprofloxacin and electrocatalysis of methanol, J. Mater. Sci. Mater. Electron. 30 (2019) 10172–10182, https://doi.org/10.1007/s10854-019-01353-6
[16] M. Kuang, J. Zhang, W. Wang, J. Chen, Y. Cao, R. Liu, J. Wang, Z. Ji, The effect of support on the structure and photocatalytic activity of ternary ZnO-$ZnFe2O_4$/palygorskite composite photocatalysts, Adv. Powder Technol. 31 (2020) 1–10, https://doi.org/10.1016/j.apt.2019.08.030
[17] Y. Yang, J. Cui, H. Jin, F. Cao, A three-dimensional (3D) structured Bi_2WO_6-palygorskite composite and their enhanced visible light photocatalytic property, Sep. Purif. Technol. 205 (2018) 130–139, https://doi.org/10.1016/j.seppur.2018.05.027
[18] E. Ruiz-Hitzky, M. Darder, F.M. Fernandes, B. Wicklein, A.C.S. Alcântara, P. Aranda, Fibrous clays based bionanocomposites, Prog. Polym. Sci. 38 (2013) 1392–1414, https://doi.org/10.1016/j.progpolymsci.2013.05.004
[19] M. Kuang, J. Zhang, W. Wang, J. Chen, Y. Cao, J. Wang, Z. Ji, Ternary Ag-deposited TiO_2/palygorskite composites with synergistic effect for enhanced photocatalytic activity, Solid State Sci. 97 (2019) 106015, https://doi.org/10.1016/j.solidstatesciences.2019.106015
[20] M. Thiruppathi, K. Selvakumar, M. Arunpandian, K. Thirumalai, C. Ramalingan, M. Swaminathan, E.R. Nagarajan, An affordable photocatalyst for pharmaceuticals and superior electrocatalyst for methanol oxidation – a dual role by $CuWO_4$ anchored bentonite clay, Colloids Surf. A Physicochem. Eng. Asp. 563 (2019) 148–159, https://doi.org/10.1016/j.colsurfa.2018.12.006
[21] J. Luo, G. Duan, W. Wang, Y. Luo, X. Liu, Size-controlled synthesis of palygorskite/Ag3PO4 nanocomposites with enhanced visible-light photocatalytic performance, Appl. Clay Sci. 143 (2017) 273–278, https://doi.org/10.1016/j.clay.2017.04.004
[22] J. Luo, Y. Luo, J. Yao, M. Zhang, S. Chen, X. Liu, Composite microsphere resulting from assembly of BiOCl nanosheets and palygorskite nanorods for enhanced photocatalytic activity, Appl. Clay Sci. 168 (2019) 450–458, https://doi.org/10.1016/j.clay.2018.12.002
[23] A. Kumar, Y. Kuang, Z. Liang, X. Sun, Microwave chemistry, recent advancements, and eco-friendly microwave-assisted synthesis of nanoarchitectures and their applications: a review, Mater. Today Nano 11 (2020) 100076, https://doi.org/10.1016/j.mtnano.2020.100076
[24] R.K. Singh, R. Kumar, D.P. Singh, R. Savu, S.A. Moshkalev, Progress in microwave-assisted synthesis of quantum dots (graphene/carbon/semiconducting) for bioapplications: a review, Mater. Today Chem. 12 (2019) 282–314, https://doi.org/10.1016/j.mtchem.2019.03.001
[25] P. Ribao, J. Corredor, M.J. Rivero, I. Ortiz, Role of reactive oxygen species on the activity of noble metal-doped TiO_2 photocatalysts, J. Hazard. Mater. 372 (2019) 45–51, https://doi.org/10.1016/j.jhazmat.2018.05.026
[26] Y. Zhang, J. Zhou, J. Chen, X. Feng, W. Cai, Rapid degradation of tetracycline hydrochloride by heterogeneous photocatalysis coupling persulfate oxidation with MIL-53(Fe) under visible light irradiation, J. Hazard. Mater. 392 (2020) 122–315, https://doi.org/10.1016/j.jhazmat.2020.122315
[27] U.G. Akpan, B.H. Hameed, Parameters affecting the photocatalytic degradation of dyes using TiO_2-based photocatalysts: a review, J. Hazard. Mater. 170 (2009) 520–529, https://doi.org/10.1016/j.jhazmat.2009.05.039

[28] X. Su, D. Wu, Facile construction of the phase junction of BiOBr and $Bi_4O_5Br_2$ nanoplates for ciprofloxacin photodegradation, Mater. Sci. Semicond. Process. 80 (2018) 123–130, https://doi.org/10.1016/j.mssp.2018.02.034
[29] L. Leng, L. Wei, Q. Xiong, S. Xu, W. Li, S. Lv, Q. Lu, L. Wan, Z. Wen, W. Zhou, Use of microalgae based technology for the removal of antibiotics from wastewater: a review, Chemosphere 238 (2020) 124680, https://doi.org/10.1016/j.chemosphere.2019.124680
[30] R. Anjali, S. Shanthakumar, Insights on the current status of occurrence and removal of antibiotics in wastewater by advanced oxidation processes, J. Environ. Manag. 246 (2019) 51–62, https://doi.org/10.1016/j.jenvman.2019.05.090
[31] S. Giannakis, S. Watts, S. Rtimi, C. Pulgarin, Solar light and the photo-Fenton process against antibiotic resistant bacteria in wastewater: a kinetic study with a Streptomycin-resistant strain, Catal. Today 313 (2018) 86–93, https://doi.org/10.1016/j.cattod.2017.10.033
[32] A.Í.S. Morais, W.V. Oliveira, V.V. De Oliveira, L.M.C. Honorio, F.P. Araujo, R.D.S. Bezerra, P.B.A. Fechine, B.C. Viana, M.B. Furtini, E.C. Silva-Filho, J.A. Osajima, Semiconductor supported by palygorskite and layered double hydroxides clays to dye discoloration in solution by a photocatalytic process, J. Environ. Chem. Eng. 7 (2019) 103–431, https://doi.org/10.1016/j.jece.2019.103431
[33] E.L.S. Souza, J.C. Sczancoski, I.C. Nogueira, M.A.P. Almeida, M.O. Orlandi, M.S. Li, R.A.S. Luz, M.G.R. Filho, E. Longo, L.S. Cavalcante, Structural evolution, growth mechanism and photoluminescence properties of $CuWO_4$ nanocrystals, Ultrason. Sonochem. 38 (2017) 256–270, https://doi.org/10.1016/j.ultsonch.2017.03.007
[34] W. Dong, Y. Lu, W. Wang, L. Zong, Y. Zhu, Y. Kang, A. Wang, A new route to fabricate high-efficient porous silicate adsorbents by simultaneous inorganic-organic functionalization of low-grade palygorskite clay for removal of Congo red, Microporous Mesoporous Mater. 277 (2019) 267–276, https://doi.org/10.1016/j.micromeso.2018.11.013
[35] J. Chen, W. Luo, A. Guo, T. Luo, C. Lin, H. Li, L. Jing, Preparation of a novel carboxylate-rich palygorskite as an adsorbent for Ce^{3+} from aqueous solution, J. Colloid Interface Sci. 512 (2018) 657–664, https://doi.org/10.1016/j.jcis.2017.09.107
[36] A.M.B.M. Oliveira, L.F.O. Coelho, S.S.S. Gomes, I.F. Costa, M.G. Fonseca, K.S. De Sousa, J.G.P. Espínola, E.C. Da Silva Filho, Brazilian palygorskite as adsorbent for metal ions from aqueous solution - kinetic and equilibrium studies, Water Air Soil Pollut. 224 (2013) 1687, https://doi.org/10.1007/s11270-013-1687-x
[37] W. Wang, A. Wang, Palygorskite Nanomaterials: Structure, Properties, and Functional Applications, Elsevier Inc., 2019, https://doi.org/10.1016/b978-0-12-814533-3.00002-8
[38] T.T. Basiev, A.A. Sobol, Y.K. Voronko, P.G. Zverev, Spontaneous Raman spectroscopy of tungstate and molybdate crystals for Raman lasers, Opt. Mater. 15 (2000) 215–216, https://doi.org/10.1016/S0925-3467(00)00037-9
[39] D.A. McKeown, J.E. Post, E.S. Etz, Vibrational analysis of palygorskite and sepiolite, Clays Clay Miner. 50 (2002) 667–680, https://doi.org/10.1346/000986002320679549
[40] S. Medidi, S. Markapurapu, M.R. Kotupalli, R.K.R. Chinnam, V.M. Susarla, H.B. Gandham, P.D. Sanasi, Visible light photocatalytic degradation of methylene blue and malachite green dyes with $CuWO_4$-GO nano composite, Mod. Res. Catal. 7 (2018) 17–34, https://doi.org/10.4236/mrc.2018.72002
[41] F. Sedighi, M. Esmaeili-Zare, A. Sobhani-Nasab, M. Behpour, Synthesis and characterization of $CuWO_4$ nanoparticle and $CuWO_4$/NiO nanocomposite using co-precipitation method; application in photodegradation of organic dye in water, J. Mater. Sci. Mater. Electron. 29 (2018) 13737–13745, https://doi.org/10.1007/s10854-018-9504-3
[42] X. Li, W. Zhu, X. Lu, S. Zuo, C. Yao, C. Ni, Integrated nanostructures of CeO_2/attapulgite/g-C_3N_4 as efficient catalyst for photocatalytic desulfurization: mechanism, kinetics and influencing factors, Chem. Eng. J. 326 (2017) 87–98, https://doi.org/10.1016/j.cej.2017.05.131
[43] J. Lian, Q. Ouyang, P.E. Tsang, Z. Fang, Fenton-like catalytic degradation of tetracycline by magnetic palygorskite nanoparticles prepared from steel pickling waste liquor, Appl. Clay Sci. 182 (2019) 105–273, https://doi.org/10.1016/j.clay.2019.105273
[44] F.R.G.V. Rosendo, L.I.F. Pinto, I.S. de Lima, P. Trigueiro, L.M. d C. Honório, M.G. Fonseca, E.C. Silva-Filho, A.B. Ribeiro, M.B. Furtini, J.A. Osajima, Antimicrobial efficacy of building material based on ZnO/palygorskite against Gram-negative and Gram-positive bacteria, Appl. Clay Sci. 188 (2020) 105499, https://doi.org/10.1016/j.clay.2020.105499
[45] M. Akkari, P. Aranda, C. Belver, J. Bedia, A. Ben Haj Amara, E. Ruiz-Hitzky, Reprint of ZnO/sepiolite heterostructured materials for solar photocatalytic degradation of pharmaceuticals in wastewater, Appl. Clay Sci. 160 (2018) 3–8, https://doi.org/10.1016/j.clay.2018.02.027
[46] Z. Abbas, R.A. Soomro, N.H. Kalwar, M. Tunesi, M. Willander, S. Karakuş, A. Kilislioğlu, In situ growth of $CuWO_4$ nanospheres over graphene oxide for photoelectrochemical (PEC) immunosensing of clinical biomarker, Sensors 20 (2020) 148, https://doi.org/10.3390/s20010148
[47] K. Aneesh, C.S.R. vusa, S. Berchmans, Enhanced peroxidase-like activity of CuWO4 nanoparticles for the detection of NADH and hydrogen peroxide, Sens. Actuators B Chem. 253 (2017) 723–730, https://doi.org/10.1016/j.snb.2017.06.175
[48] Y. Tang, N. Rong, F. Liu, M. Chu, H. Dong, Y. Zhang, P. Xiao, Enhancement of the photoelectrochemical performance of $CuWO_4$ films for water splitting by hydrogen treatment, Appl. Surf. Sci. 361 (2016) 133–140, https://doi.org/10.1016/j.apsusc.2015.11.129
[49] N. Le Minh Tri, D.Q. Trung, D. Van Thuan, N.T. Dieu Cam, T. Al Tahtamouni, T.D. Pham, D.S. Duc, M.H. Thanh Tung, H. Van Ha, N.H. Anh Thu, H.T. Trang, The advanced photocatalytic performance of V doped $CuWO_4$ for water splitting to produce hydrogen, Int. J. Hydrog. Energy 45 (2020) 18186–18194, https://doi.org/10.1016/j.ijhydene.2019.06.132
[50] L. Tan, A. Tang, Y. Zou, M. Long, Y. Zhang, J. Ouyang, J. Chen, Sb_2Se_3 assembling Sb_2O_3@attapulgite as an emerging composites for catalytic hydrogenation of p-nitrophenol, Sci. Rep. 7 (2017) 1–11, https://doi.org/10.1038/s41598-017-03281-z
[51] Y. Shi, Q. Zhang, X. Zhu, J. Wang, J. Chen, Y. Shi, Z. Yang, H. Cui, Y. Hu, L. Zhang, K. Wang, Palygorskite supported $BiVO_4$ photocatalyst for tetracycline hydrochloride removal, Appl. Clay Sci. 137 (2017) 249–258, https://doi.org/10.1016/j.clay.2016.12.035
[52] X. Xie, M. Liu, C. Wang, L. Chen, J. Xu, Y. Cheng, H. Dong, F. Lu, W.H. Wang, H. Liu, W. Wang, Efficient photo-degradation of dyes using $CuWO_4$ nanoparticles with electron sacrificial agents: a combination of experimental and theoretical exploration, RSC Adv. 6 (2016) 953–959, https://doi.org/10.1039/c5ra18788e
[53] H. Dong, Y. Li, D. Gao, M. Zhou, X. Hu, H. Peng, L. Yang, J. He, Y. Zhang, P. Xiao, Efficient self-assembly solvothermal synthesis of octahedral $CuWO_4$ microstructures assisted by ethylene glycol, J. Alloy. Compd. 785 (2019) 660–668, https://doi.org/10.1016/j.jallcom.2019.01.224
[54] W. Ding, X. Wu, Q. Lu, Structure and photocatalytic activity of thin-walled $CuWO_4$ nanotubes: an experimental and DFT study, Mater. Lett. 253 (2019) 323–326, https://doi.org/10.1016/j.matlet.2019.06.109
[55] K. Liu, Z. Tong, Y. Muhammad, G. Huang, H. Zhang, Z. Wang, Y. Zhu, R. Tang, Synthesis of sodium dodecyl sulfate modified BiOBr/magnetic bentonite photocatalyst with Three-dimensional parterre like structure for the enhanced photodegradation of tetracycline and ciprofloxacin, Chem. Eng. J. 388 (2020) 124374, https://doi.org/10.1016/j.cej.2020.124374
[56] Y. Li, Y. Fu, M. Zhu, Green synthesis of 3D tripyramid TiO_2 architectures with assistance of aloe extracts for highly efficient photocatalytic degradation of antibiotic ciprofloxacin, Appl. Catal. B Environ. 220 (2020) 118–149, https://doi.org/10.1016/j.apcatb.2019.118149
[57] J. Ma, C. Zhu, J. Lu, H. Liu, L. Huang, T. Chen, D. Chen, Catalytic degradation of gaseous benzene by using TiO_2/goethite immobilized on palygorskite: preparation, characterization and mechanism, Solid State Sci. 49 (2015) 1–9, https://doi.org/10.1016/j.solidstatesciences.2015.09.007
[58] J. Ma, Q. Liu, L. Zhu, J. Zou, K. Wang, M. Yang, S. Komarneni, Visible light photocatalytic activity enhancement of Ag_3PO_4 dispersed on exfoliated bentonite for degradation of rhodamine B, Appl. Catal. B Environ. 182 (2016) 26–32, https://doi.org/10.1016/j.apcatb.2015.09.004
[59] M. Thommes, K. Kaneko, A.V. Neimark, J.P. Olivier, F. Rodriguez-Reinoso, J. Rouquerol, K.S.W. Sing, Physisorption of gases, with special reference to the evaluation of surface area and pore size distribution (IUPAC Technical Report), Pure Appl. Chem. 87 (2015) 1051–1069, https://doi.org/10.1515/pac-2014-1117
[60] N. Askari, M. Beheshti, D. Mowla, M. Farhadian, Fabrication of $CuWO_4/Bi_2S_3$/ZIF67 MOF: a novel double Z-scheme ternary heterostructure for boosting visible-light photodegradation of antibiotics, Chemosphere 251 (2020) 126–453, https://doi.org/10.1016/j.chemosphere.2020.126453
[61] Y. Qin, H. Li, J. Lu, Y. Yan, Z. Lu, X. Liu, Enhanced photocatalytic performance of MoS2 modified by AgVO 3 from improved generation of reactive oxygen species, Chin. J. Catal. 39 (2018) 1470–1483, https://doi.org/10.1016/S1872-2067(18)63111-0
[62] D. Bohra, W.A. Smith, Improved charge separation via Fe-doping of copper tungstate photoanodes, Phys. Chem. Chem. Phys. 17 (2015) 9857–9866, https://doi.org/10.1039/c4cp05565a
[63] D. Hu, P. Diao, D. Xu, M. Xia, Y. Gu, Q. Wu, C. Li, S. Yang, Copper(II) tungstate nanoflake array films: sacrificial template synthesis, hydrogen treatment, and their application as photoanodes in solar water splitting, Nanoscale 8 (2016) 5892–5901, https://doi.org/10.1039/c5nr09210h
[64] Y. Luo, J. Luo, Y. Hua, J. Yao, S. ming Chen, X. Liu, One pot synthesis of α-AgVO3/palygorskite nanocomposites with enhanced photocatalytic activity using triple roles of palygorskite: supporter, dispersant and growth-directing agent, Dalton Trans. 47 (2018) 16855–16861, https://doi.org/10.1039/c8dt02636j
[65] E. Parvizi, R. Tayebee, E. Koushki, M.F. Abdizadeh, B. Maleki, P. Audebert, L. Galmiche, Photocatalytic efficacy of supported tetrazine on MgZnO nanoparticles for the heterogeneous photodegradation of methylene blue and ciprofloxacin, RSC Adv. 9 (2019) 23818–23831, https://doi.org/10.1039/c9ra04702f
[66] C.J. Wang, Z. Li, W.T. Jiang, J.S. Jean, C.C. Liu, Cation exchange interaction between antibiotic ciprofloxacin and montmorillonite, J. Hazard. Mater. 183 (2010) 309–314, https://doi.org/10.1016/j.jhazmat.2010.07.025
[67] C.C. Lin, C.Y. Lee, Adsorption of ciprofloxacin in water using Fe_3O_4 nanoparticles formed at low temperature and high reactant concentrations in a rotating packed bed with co-precipitation, Mater. Chem. Phys. 240 (2020) 122049, https://doi.org/10.1016/j.matchemphys.2019.122049
[68] X. Li, W. Wang, J. Dou, J. Gao, S. Chen, X. Quan, H. Zhao, Dynamic adsorption of ciprofloxacin on carbon nanofibers: quantitative measurement by in situ fluorescence, J. Water Process Eng. 9 (2016) e14–e20, https://doi.org/10.1016/j.jwpe.2014.12.006
[69] A. Ashiq, B. Sarkar, N. Adassooriya, J. Walpita, A.U. Rajapaksha, Y.S. Ok, M. Vithanage, Sorption process of municipal solid waste biochar-montmorillonite composite for ciprofloxacin removal in aqueous media, Chemosphere 236 (2019) 124–384, https://doi.org/10.1016/j.chemosphere.2019.124384
[70] H. Rasoulzadeh, A. Mohseni-Bandpei, M. Hosseini, M. Safari, Mechanistic investigation of ciprofloxacin recovery by magnetite–imprinted chitosan nanocomposite: isotherm, kinetic, thermodynamic and reusability studies, Int. J. Biol. Macromol. 133 (2019) 712–721, https://doi.org/10.1016/j.ijbiomac.2019.04.139
[71] T.M. Berhane, J. Levy, M.P.S. Krekeler, N.D. Danielson, Adsorption of bisphenol A and ciprofloxacin by palygorskite-montmorillonite: effect of granule size,

solution chemistry and temperature, Appl. Clay Sci. 132–133 (2016) 518–527, https://doi.org/10.1016/j.clay.2016.07.023
[72] A. Mishra, A. Mehta, M. Sharma, S. Basu, Enhanced heterogeneous photodegradation of VOC and dye using microwave synthesized TiO_2/Clay nanocomposites: a comparison study of different type of clays, J. Alloy. Compd. 694 (2017) 574–580, https://doi.org/10.1016/j.jallcom.2016.10.036
[73] M. Thiruppathi, K. Leeladevi, C. Ramalingan, K.C. Chen, E.R. Nagarajan, Construction of novel biochar supported copper tungstate nanocomposites: a fruitful divergent catalyst for photocatalysis and electrocatalysis, Mater. Sci. Semicond. Process. 106 (2020) 104–766, https://doi.org/10.1016/j.mssp.2019.104766
[74] A. Raja, P. Rajasekaran, K. Selvakumar, M. Arunpandian, K. Kaviyarasu, S. Asath Bahadur, M. Swaminathan, Visible active reduced graphene oxide-$BiVO_4$-ZnO ternary photocatalyst for efficient removal of ciprofloxacin, Sep. Purif. Technol. 233 (2020) 115–996, https://doi.org/10.1016/j.seppur.2019.115996
[75] J.B. Sambur, T.Y. Chen, E. Choudhary, G. Chen, E.J. Nissen, E.M. Thomas, N. Zou, P. Chen, Sub-particle reaction and photocurrent mapping to optimize catalyst-modified photoanodes, Nature 530 (2016) 77–80, https://doi.org/10.1038/nature16534
[76] A.V. de Bairros, D.B. Pereira, E.W.F. Cordeiro, C.S. Paim, F.E.B. da Silva, M.D. Malesuik, F.R. Paula, Evaluation of the influence of fluoroquinolone chemical structure on stability: forced degradation and in silico studies, Braz. J. Pharm. Sci. 54 (2018) 1–10, https://doi.org/10.1590/s2175-97902018000100188
[77] Y.H. Chiu, T.F.M. Chang, C.Y. Chen, M. Sone, Y.J. Hsu, Mechanistic insights into photodegradation of organic dyes using heterostructure photocatalysts, Catalysts 9 (2019) 430, https://doi.org/10.3390/catal9050430
[78] H. Zhao, Y. Zhang, G. Li, F. Tian, H. Tang, R. Chen, Rhodamine B-sensitized BiOCl hierarchical nanostructure for methyl orange photodegradation, RSC Adv. 6 (2016) 7772–7779, https://doi.org/10.1039/c5ra24887f
[79] H.G. Oliveira, L.H. Ferreira, R. Bertazzoli, C. Longo, Remediation of 17-α-ethinylestradiol aqueous solution by photocatalysis and electrochemically-assisted photocatalysis using TiO_2 and TiO_2/WO_3 electrodes irradiated by a solar simulator, Water Res. 72 (2015) 305–314, https://doi.org/10.1016/j.watres.2014.08.042
[80] K.K. Kefeni, B.B. Mamba, Photocatalytic application of spinel ferrite nanoparticles and nanocomposites in wastewater treatment: review, Sustain. Mater. Technol. 23 (2020) e00140, https://doi.org/10.1016/j.susmat.2019.e00140
[81] A. Salma, S. Thoröe-Boveleth, T.C. Schmidt, J. Tuerk, Dependence of transformation product formation on pH during photolytic and photocatalytic degradation of ciprofloxacin, J. Hazard. Mater. 313 (2016) 49–59, https://doi.org/10.1016/j.jhazmat.2016.03.010